

# Computational Methods for Amorphous Semiconductor Devices

Ember L. Sikorski<sup>a</sup>

<sup>a</sup>*Boise State University*

---

## Abstract

- DOS
  - structural modeling
- 

## 1. Introduction

### 1.1. Why model amorphous semiconductors?

### 1.2. How can we model amorphous semiconductors?

Computational modeling spans length scales from the order of meters, that we experience, to the order of Angstroms, that atoms experience. Due to this vast range of length scales, no one method can address all properties. Following, computational methods are broken down into four main categories (Figure 1): First principles or *ab initio*, molecular dynamics (MD), mesoscale methods such as Monte Carlo (MC), and continuum methods such as finite element analysis (FEA)[1].

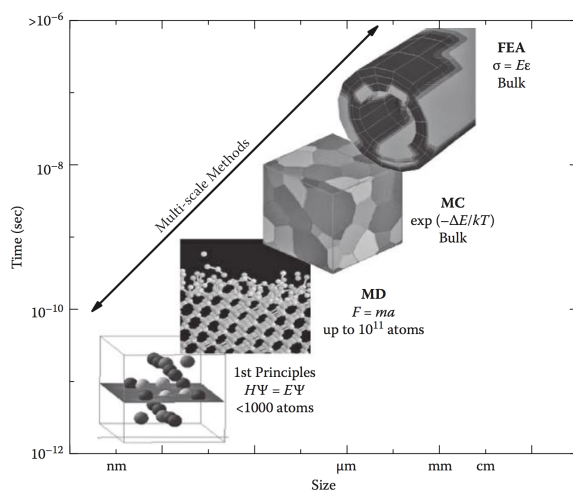


Figure 1: Overview of computational methods with respect to time and size capabilities. [1]

## 2. First Principles

First principles, or *ab initio*, modeling is derived solely from quantum mechanics and considers the nuclei and atoms of a system. The term "first principles" refers to the models ability to solve for electronic and structural properties knowing only the constituent atomic species or, rather, no experimental input. The method is based on the Schrödinger's equation. However, this equation can only be analytically solved for hydrogen. To extend its applicability, several assumptions and approximations must be made to yield density functional theory (DFT).

In short, DFT does not consider gravity, relativity, or excited states [1]. The nuclei and electrons are considered separately, known as the Born-Oppenheimer approximation, as nuclei are 10,000 times more massive than electrons, in the case of semiconductors, and the electrons will instantaneously move with them. These simplifications yield the following Hamiltonian:

$$\hat{H} = -\frac{1}{2} \sum_i^n \nabla_i^2 - \sum_I^N \sum_i^n \frac{Z_I}{|\vec{r}_{Ii}|} + \sum_{i \neq j}^n \frac{1}{|\vec{r}_{ij}|} \quad (1)$$

where  $N$  is the number of nuclei,  $n$  is the number of electrons,  $Z_I$  is the charge of the nuclei,  $\nabla^2$  is the Laplacian operator, and  $\vec{r}$  is the position. The first term is the kinetic energy, the second is the potential between electrons and nuclei, and the third is the potential between electrons. Energy is calculated by taking the expectation value of the Hamiltonian:

$$E = \sum_{i,j} \int \Psi_i^*(\vec{r}) \left( -\frac{1}{2} \sum_i^n \nabla_i^2 - \sum_I^N \sum_i^n \frac{Z_I}{|\vec{r}_{Ii}|} + \sum_{i \neq j}^n \frac{1}{|\vec{r}_{ij}|} \right) \Psi_i(\vec{r}) d\vec{r} \quad (2)$$

The Kohn-Sham approach is applied to turn the  $n$ -electron system into a fictitious system of one-electrons. Solving the Kohn-Sham Hamiltonian yield the Kohn-Sham orbitals  $\phi_i(\vec{r})$ :

$$\left[ -\frac{1}{2} \nabla^2 + U_{eff}(\vec{r}) \right] \phi_i(\vec{r}) = \varepsilon_i \phi_i(\vec{r}) \Rightarrow \hat{H}_{KS} \phi_i = \varepsilon_i \phi_i(\vec{r}) \quad , \quad (3)$$

where  $\varepsilon_i$  are the Kohn-Sham eigenvalues. The electron density is then found by summing over the squares of the non-interacting Kohn Sham orbitals:

$$\rho(r) = \sum_i |\phi_i(r)|^2 \quad . \quad (4)$$

The third term of the Hamiltonian, the potential energy between electrons, is split into Hartree energy and exchange-correlation energy. The Hartree energy is the potential felt on each electron by a homogeneous electron gas of all the other electrons. Exchange energy describes the interaction of same spin electrons and correlation energy describes the interaction of different spin electrons.

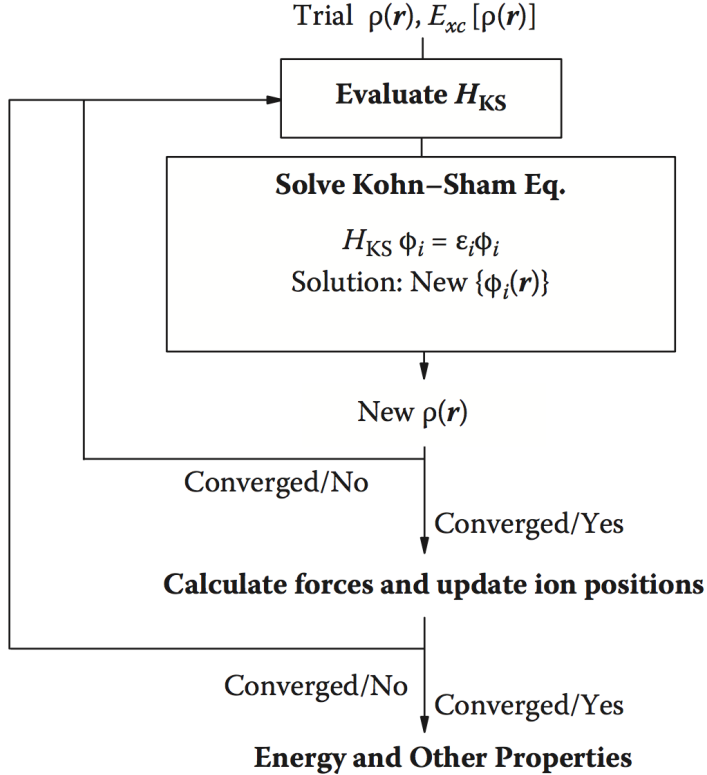


Figure 2: Self-consistent framework (SFC) loop used in DFT [1].

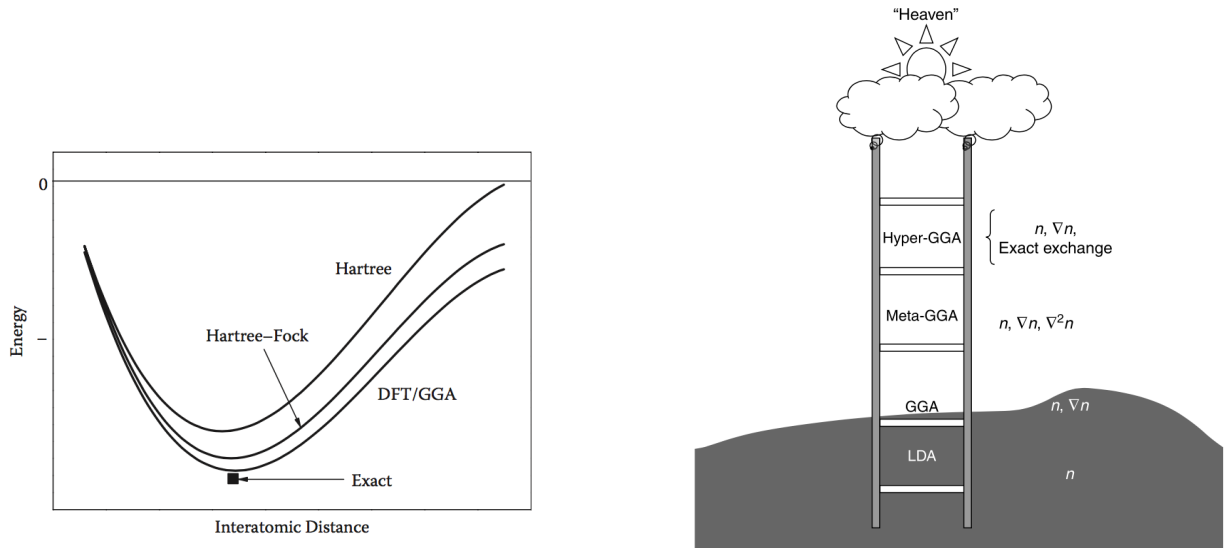


Figure 3: Energy schematic [1] (left) and Jacob's ladder depiction [4] of various functionals.

Meta-GGA, also referred to as hybrid functionals, combine Hartree Fock with DFT functionals. Going up the ladder represents increasing accuracy when compared with experiment, but it is

done at computational cost. Any functional at the third rung or above is at least ten times as expensive as GGA [1]. Though the Jacob's ladder is presented as a linear progression between functionals, this is a large simplification and the accuracy of a functional is often system-dependent. Another important consideration when selecting a functional is whether it is nonempirical - based on constraints of the Kohn-Sham functional - or empirical - parameterized by experiment [4]. The B3LYP functional, for example, is an empirical potential fitted to atomization energies, ionization potentials, and other experimental values [1]. It excels in describing molecular systems, van der Waals interactions, and rapidly fluctuating electron densities. However, this method is not always well suited for metals and semiconductors [5].

### 2.1. Photoluminescence in amorphous perovskites

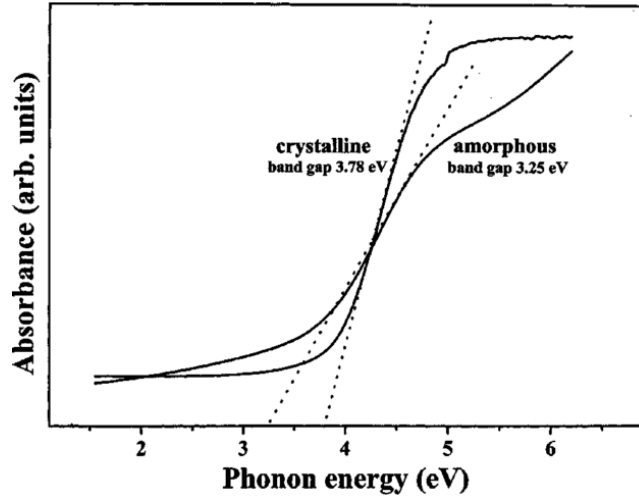


FIG. 4. UV-visible absorbance spectra for crystalline and amorphous BST thin films.

Figure 4: UV-visible absorbance spectra for crystalline and amorphous  $\text{Ba}_{0.5}\text{Sr}_{0.5}\text{TiO}_3$  films from Longo et al. [6]

Longo et al. [6] used DFT to determine the origin of photoluminescence in their amorphous titanates. They chose crystalline and amorphous  $\text{Ba}_{0.5}\text{Sr}_{0.5}\text{TiO}_3$  (BST) for computational analysis using the B3LYP functional. From x-ray absorption near edge spectra (XANES), they determined the amorphous titanates contained both fivefold and sixfold oxygen-titanium coordination. In order to create this coordination, they shifted the Ti atom by  $0.5 \text{ \AA}$ , as shown in Fig. YYY. From the band gap in Fig. YYY, the indirect bandgap in crystalline BST is equal to 3.78 eV, in agreement with the optical bandgap found in experiment (Figure. YYY). For amorphous BST, this indirect bandgap decreases to 3.06 eV. The LDOS in Fig. YYY show the valence band is made up of O states while the conduction band is made of Ti states. The authors note covalent bonding occurs between Ti and O, through the overlap of Ti 3d states and O 2p states. The nature of the bonding is further realized in Fig. YYY(a). A valley exists in the surface plot between Ba and Sr, indicating ionic bonding. Conversely, the charge density between Ti and O is higher and can additionally by

seen in the contour map as exhibiting regions of the same charge. These characteristics point to covalent bonding. Fig. YYY(b) emphasizes the distinction between the Ti-O bonds in crystalline an amorphous BST: the covalent bonds are weaker in amorphous BST as the contour map shows reduced regions of the same charge density. These results suggest that the change in the Urbach tail of the absorption spectra is due to the disorder in the amorphous structure which leads to localized states in the O 2p orbitals.

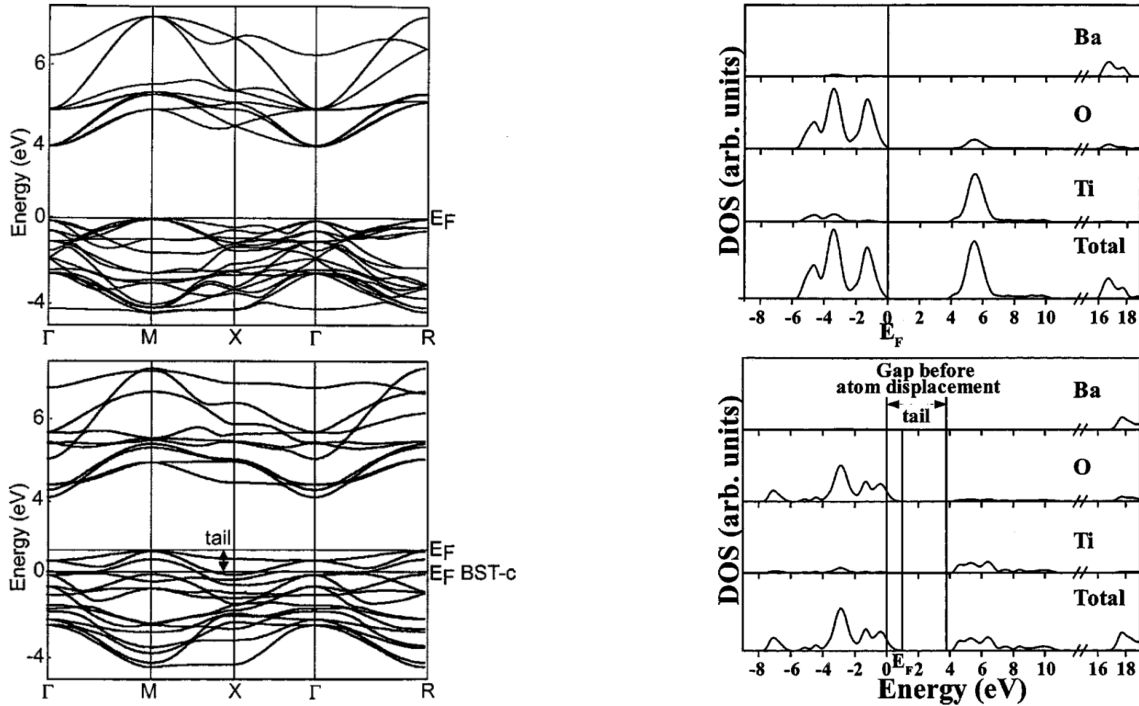


Figure 5: Calculated band structure (left) and density of states (right) from Longo et al. [6] for crystalline (top) and amorphous (bottom)  $\text{Ba}_{0.5}\text{Sr}_{0.5}\text{TiO}_3$ .

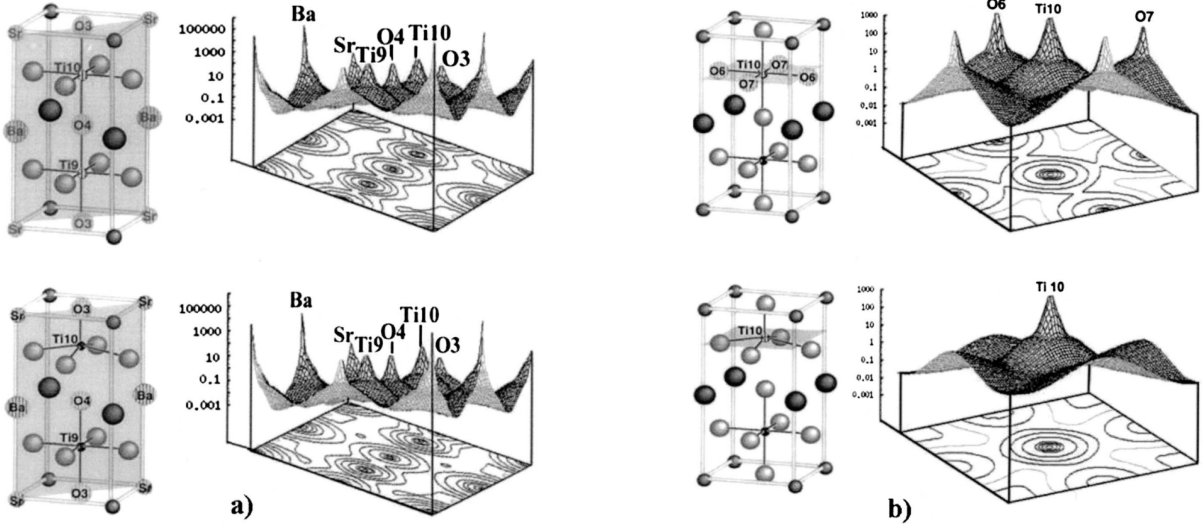


Figure 6: Charge density from surface and contour plots from Longo et al. [6] for crystalline and amorphous  $\text{Ba}_{0.5}\text{Sr}_{0.5}\text{TiO}_3$ . (a) shows the vertical diagonal plane and (b) shows a horizontal plane.

Though the band gap results of Longo et al. agree well with their experimental data, the structure they modeled is not entirely amorphous. Due to their small unit cell of  $1 \times 1 \times 2$ , this creates a periodic structure in which half of the Ti have distorted local bonding. If there were greater distribution of bond lengths and types, it is likely further details in the photoluminescence mechanism could be unearthed.

Additionally, the B3LYP is a partially empirical functional [5]. Due to the fixed nature of empirical potentials, this method may struggle in accurately representing the system if the system exhibits any anisotropy [7]. Paier et al. [5] have shown that B3LYP performs poorly for metals and small gap semiconductors, which would be better described with nonempirical hybrid functionals such as PBE0 and HSE03. At the high computational cost of a hybrid functional, a nonempirical function may be better suited for such a study.

### 3. Molecular Dynamics

Molecular Dynamics (MD) is a classical method built off of

$$\vec{F} = m\vec{a} \quad . \quad (5)$$

Atoms are the smallest building block, represented as a sphere with a point mass [1]. To calculate desired properties, atoms are allowed to “relax” to their respective equilibrium distances, by moving down along the negative energy gradient:

$$\vec{F} = -\nabla U \quad . \quad (6)$$

A calculation begins with a set of starting atomic coordinates. The energy is calculated and the atoms are adjusted, following the gradient, to a more stable position. The energy is again calculated and compared to the previous step. This process continues until the differences between

subsequent energy values reaches a predetermined stopping value, e.g. a difference of  $1 \times 10^{-4}$  eV or less.

This method requires selection of so-called pair-potentials, which describe how atom  $i$  interacts with atom  $j$ . The simplest potential is the Lennard-Jones potential:

$$U_{ij}(r) = 4\epsilon \left[ \left( \frac{\sigma}{r} \right)^{12} - \left( \frac{\sigma}{r} \right)^6 \right] , \quad (7)$$

where  $\epsilon$  is the depth of the energy well and  $\sigma$  is the interatomic distance at which the potential is zero. However, this potential can only describe the interactions between atoms of the same element. In order to perform calculations on the majority of systems of interest, more complex pair-potentials are needed. Numerous potentials have been created, such as Embedded Atom Method (EAM) potentials which work for many metals and Tersoff potentials for covalent solids.

An alternative method necessary for our discussion of AIMD in Section YYY is the Lagrangian:

$$L = K - U = \frac{1}{2} \sum_{i=1}^{3N} m_i v_i^2 - U(r_1, \dots, r_{3N}) , \quad (8)$$

where  $K$  is the kinetic energy,  $U$  is the potential energy, and  $N$  is the number of atoms.

### 3.1. MD for the structure of alumina

Gutiérrez et al. [3] used MD to investigate the structure of alumina. With the success of alloys and metals such as stainless steel, Ti, and Al largely attributed to their oxide layer, determining the structure of this oxide aids understanding of the passivation process. Gutiérrez used the pairwise potential

$$U(r_{ij}) = \frac{q_i q_j}{r_{ij}} - \frac{C_i C_j}{r_{ij}^6} + D(B_i + B_j) \exp \left( \frac{A_i + A_j - r_{ij}}{B_i + B_j} \right) , \quad (9)$$

where  $r_{ij}$  is the interatomic distance between atoms  $i$  and  $j$ ,  $D$  is the standard force constant 4.184 kJ/Å·mol.,  $q$  is the effective charge,  $A$  is the repulsive radius,  $B$  is the softness parameter, and  $C$  is the van der Waals coefficient. This potential has been demonstrated to reproduce the structure, bulk modulus, thermal expansivities, melting temperatures, and liquid structure properties of  $\text{Al}_2\text{O}_3$ .

With a system of 1800 atoms, the researchers performed a melt-quench simulation by heating the system to 5000 K and evolving for 45 ps. Next the system was cooled to 3000 K at a rate of 1 K per 30 timesteps (1 fs). Finally, the system was allowed to equilibrate for 55 ps. Though these methods are known to be highly dependent on the melt-quench recipe, alternative initial configurations and quench rates were tested, but no discernible difference was found. To perform statistical analysis of the structure, properties were averaged over 100 configurations: the last 100 structures, each 100 fs apart.

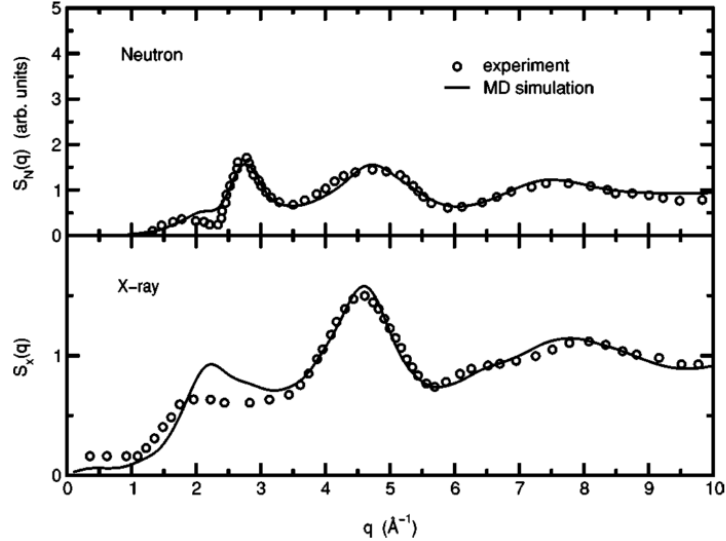


Figure 7: MD results of Gutiérrez et al. [3] compared with experimental data for neutron and x-ray static structure function of  $\text{Al}_2\text{O}_3$ .

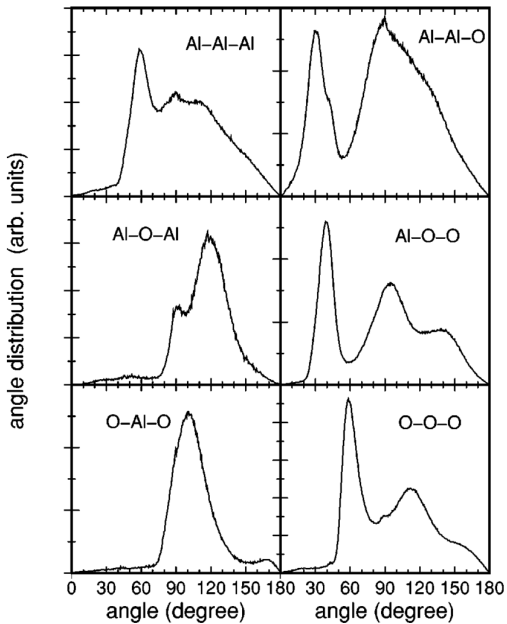


Figure 8: Results of Gutiérrez et al. [3] for bond angle distribution in amorphous  $\text{Al}_2\text{O}_3$ .

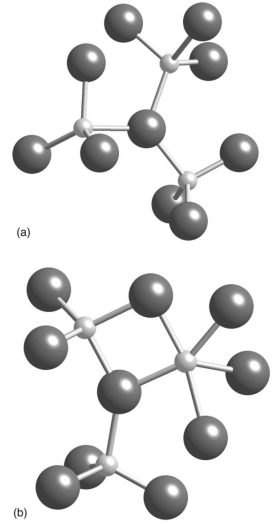


Figure 9: Model suggested by Gutiérrez et al. [3] for basic  $\text{Al}_2\text{O}_3$  units. (a) shows corner sharing tetrahedra while (b) shows edge-sharing polyhedra. Small and big spheres represent Al and O atoms, respectively.

When compared with experimental structure factor, the results are in general agreement (Figure YYY). Though at low  $q$  the results do not quite align, the simulation still shows a “prepeak,” consistent with experiment. From the bond-angle distribution shown in Figure YYY, the authors determined two structural motifs, as shown in Figure YYY.

## 4. Monte Carlo

Reverse Monte Carlo (RMC) algorithm can be used to find atomicistic models from experimental data, commonly diffraction results. This large length scale method can produce unit cells on the order of thousands of atoms. The simulation begins with a unit cell with the desired atomic species and undergoes an iterative process of random atomic movements [2]. If the movement creates a structure that better matches experiment, the movement is accepted. If the movement creates a structure yielding results less like diffraction data, the movement is rejected. Using this method in combination with DFT can help overcome the energetic barriers to atomic reconfiguration. The authors note that creating stochastic models and relaxing with DFT can create unphysical structures. To avoid this problem, White et al. [2] use an RMC algorithm that is restrained to favor simpler solutions.

The authors began with a pair distribution function (PDF) generated from a successful molecular dynamics model of a-Si referred to as WWW. Next, they created a random 512 atom unit cell and optimized the structure following

$$\chi = \frac{w_{PDF}}{N} \sum_j \sum_r \frac{[g_j(r) - g_{expt}(r)]}{r^2} + \frac{w_L}{N} \sum_{ij} L_{ij} , \quad (10)$$

where  $N$  is the total number of atoms,  $g_j(r)$  is the individual atomic radial distribution function,  $g_{expt}$  is the experimental radial distribution function,  $w_{PDF}$  is the weight of the PDF data, and  $w_L$  is the weight of the self-similarity restraint. The self-similarity is evaluated using the smooth overlap of atomic positions (SOAP) descriptor. This descriptor compares two atomic densities  $\rho_i$  and  $\rho_j$  over all rotations  $\hat{R}$  and all positions  $\vec{r}$ :

$$k_{ij} = \int d\hat{R} \left| \int d\vec{r} \rho_i(\vec{r}) \rho_j(\vec{r})(\hat{R}\vec{r}) \right|^2 . \quad (11)$$

The authors also introduced an adaptive weighting scheme to confirm both self-similarity and PDF data contributed equally throughout the refinement. This was introduced as a scaling factor

$$A = \left( \frac{w_{PDF} \chi_{PDF}}{w_L \chi_L} \right)^{0.25} , \quad (12)$$

multiplied by the previous PDF weight and divided by the previous self-similarity rate. The results of this weighting scheme are shown in Fig. YYY.

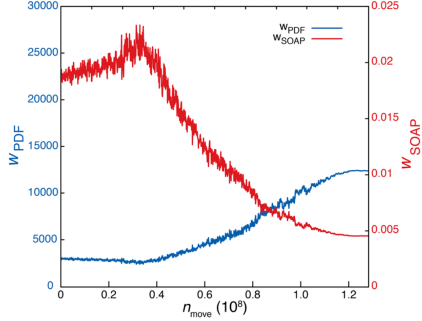


Figure 10: Evolution of weighting scheme used by White et al. [2].

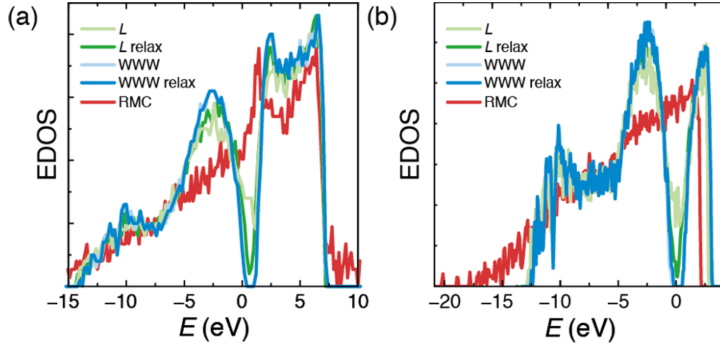


Figure 11: Electronic density of states calculated from the (a) tight-binding model and the (b) MBJ meta-GGA functional for a-Si by White et al. [2]. The density of states for unrestrained RMC is shown for comparison.

After obtaining the a-Si structure from L-constrained RMC, DFT calculations using the tight binding model were performed to obtain the electronic structure shown in Fig. YYY. The unconstrained RMC DOS is rather featureless, while L-constrained RMC qualitatively reproduces the results of WWW. The authors double checked their results with the MBJ meta-GGA functional, known to accurately reproduce electronic properties of semiconductors, to confirm the results of their tight-binding model. Relaxation led to a slight deviation from the PDF data through the elimination of dangling-bond defects and, in turn, reduction in the density of gap states. Overall, this study demonstrates the utility in using simplity constraints on atomic relaxation.

## 5. *Ab initio* Molecular Dynamics

*Ab initio* Molecular Dynamics (AIMD) refers to any calculation that advances atoms along classical trajectories based on forces calculated from DFT[4].

AIMD is an incredibly powerful method capable of adding time to a DFT simulation while still allowing for *ab initio* calculation of electronic properties. Furthermore, AIMD can circumvent the problem of metastable states, as shown for DFT+U [8]. This can be better conceptualized with the schematic of Car-Parrinello MD in Figure YYY. Instead of performing AIMD as a stepwise process in which calculating the atomic trajectories and the electronic ground state are separate,

Car and Parrinello formulated the two to run simultaneously. Their extended Lagrangian introduces the electronic degrees of freedom as fictitious dynamical variables:

$$L = \frac{1}{2} \sum_{i=1}^{3N} m_i v_i^2 - U(r_1, \dots, r_{3N}) + \frac{1}{2} \sum_j 2\mu \int d\vec{r} |\dot{\psi}(\vec{r})|^2 + L_{ortho} \quad (13)$$

The third term introduces fictitious mass,  $\mu$ , and the final term restrains the one-electron wave functions to be orthogonal. Since the total energy calculation occurs simultaneously with the atomic trajectory calculation, the energy is not quite the same as the energy calculated with pure DFT, as shown in Figure YYY. This phenomena circumvents the structure getting trapped in a metastable state, as DFT methods are known to do [9].

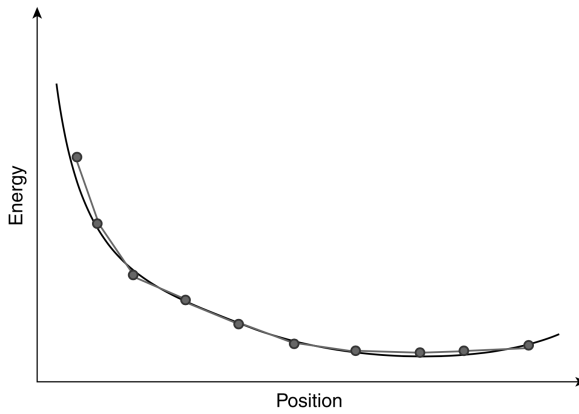


Figure 12:

Shortly after the formulation of Car-Parrinello MD, Car and Parrinello realized the utility of the method for

### 5.1. AIMD for Phase Change Memory

Raty et al. [10] used Ab Initio Molecular Dynamics to understand the structural changes associated with aging in GeTe, and the effects those changes have on performance. Inherently out of equilibrium, amorphous materials evolve with time to a lower energetic state. In the case of phase change materials, this evolution leads to higher electrical resistivity that undermines its usability in multilevel memory devices. Using AIMD, we can watch the structure evolve, but though we discussed the addition of time to DFT above, this time is still on the order of picoseconds, leaving real-time aging out of the question. Raty et al. have sidestepped this problem by creating an arrangement of structures with varying local motifs.

Their study begins with the observation that AIMD simulations of  $Ge_xSb_yTe_{1+x+y}$  alloys show tetrahedrally bonded Ge ( $Ge^T$ ) atoms in the amorphous phase, though these are absent in crystalline Ge. To investigate the effect of such homopolar bonds on GeTe properties, the authors melt-quenched GeTe along with a combination of other binary chalcogenides for use as “templates.” SiTe forms numerous  $Si^T$ , GeSe contains some  $Ge^T$ , and SnTe contains almost no tetrahedral motifs. The authors then substituted one species in each of the template compounds to form GeTe, i.e.

substituting Si in SiTe with Ge, Se in GeSe with Te, and Sn in SnTe with Ge. After substitution, the systems were subjected to a shorter additional melt-quench procedure.

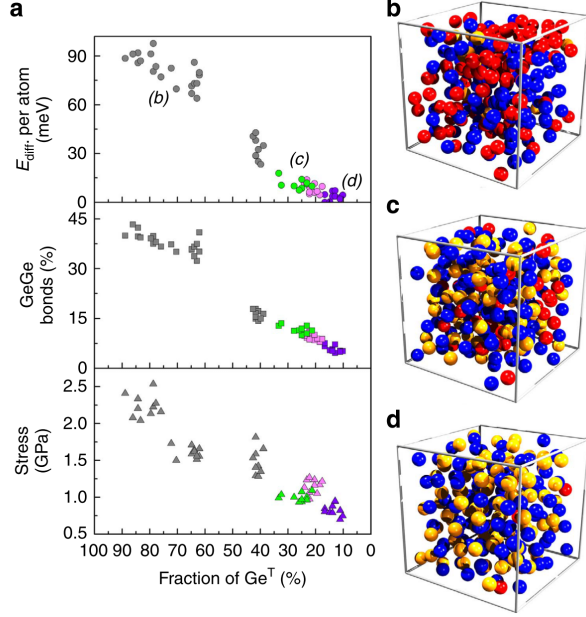


Figure 13: Results from Raty et al. [10] for (a) the energy difference per atom, fraction of homopolar GeGe bonds, and stress of the melt-quenching of GeTe (green) and chemical replacement systems SnTe (violet), GeSe (pink), and SiTe (grey). (b-d) show the atomic configurations of GeTe as labeled in the energy difference plot. Te, tetrahedral Ge, and octahedral Ge are rendered in blue, red, and orange, respectively.

The results shown in Figure. YYY indicate that the homopolar bonds reduce the stability of the system. However, homopolar bonds have a lower heat of formation in GeTe than in both GeSe and SnTe, and the melt-quench process is able to stabilize these tetrahedral motifs. In comparison to experiment, aging of phase change materials has been linked with stress relief. These results suggest that the removal of homopolar bonds contributes to this stress relief.

Raty et al. additionally calculated the changes in the electronic and optical bandgaps due to the changes in percent Ge<sup>T</sup>. Though methods of calculating optical properties are beyond the scope of this review, the results of Raty et al. for the optical bandgap in Figures. YYY(a) and YYY show increasing band gap correlated with decreasing homopolar bonds, in agreement with experiment showing band gap widening with aging. Similarly, the DOS shows an increase in electronic band gap with aging, and the disappearance of the midgap states are directly linked to the removal of homopolar bonds. The authors note that while a variety of Ge<sup>T</sup> concentrations have been modeled, this method does not yield access to the time scale of the relaxation process.

## 6. Discussion

## 7. Conclusion

know when your methods fail

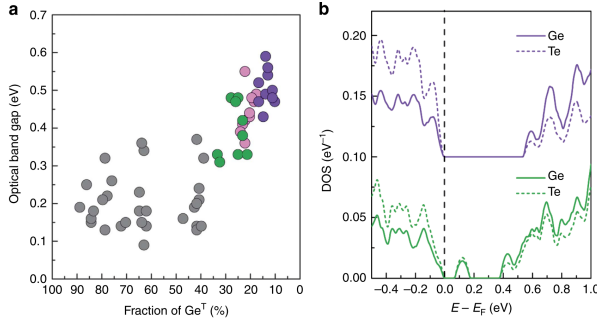


Figure 14: Results from Raty et al. [10] for (a) the relaxed amorphous GeTe structures as a function of percent Ge<sup>T</sup> and (b) the local density of states for melt-quenched GeTe (green) and substituted a-SnTe (violet).

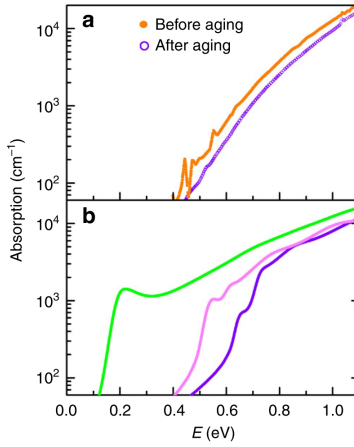


Figure 15: Results from Raty et al. [10] for (a) experimental absorption from photothermal deflection spectroscopy (PDS) and (b) calculated absorption oscillator strength for melt-quenched GeTe (green), substituted a-GeSe (pink), and substituted a-Sn-Te (violet).

- MD iff
  - isotropic
  - potential reproduces desired properties

## Notes

- Kohn Sham: A *system* of one-electrons
- Hartree: a *potential* of how each electrons feels the electron gas
- Hartree Fock: how we describe the wave functions

### 7.1. AIMD

Hohl 1991[7] - Liquid and amorphous Se

#### Computational comments

- many structural models have been proposed and often conflict
- models based solely on small differences are insufficient to explain all measured features
- even carefully constructed empirical potentials have difficulty in highly anisotropic covalent systems such as group-IVA elements.
- AIMD avoids parameterization of interatomic forces common in MD

## References

- [1] J. G. Lee, Computational Materials Science: An Introduction, CRC Press, 2012.
- [2] C. E. White, N. J. Henson, L. L. Daemen, M. Hartl, K. Page, Uncovering the True Atomic Structure of Disordered Materials: The Structure of a Hydrated Amorphous Magnesium Carbonate ( $MgCO_3 \cdot 3D_2O$ ) doi:10.1021/cm500470g.  
URL <https://pubs.acs.org/sharingguidelines>
- [3] G. Gutiérrez, B. Johansson, Molecular dynamics study of structural properties of amorphous Al<sub>2</sub>O<sub>3</sub>, Physical Review B 65 (104202) (2002) 1–9. doi:10.1103/PhysRevB.65.104202.  
URL <https://link.aps.org/doi/10.1103/PhysRevB.65.104202>
- [4] D. S. Sholl, J. A. Steckel, Density Functional Theory: A Practical Introduction, 2009.
- [5] J. Paier, M. Marsman, G. Kresse, Why does the B3LYP hybrid functional fail for metals?, The Journal of Chemical Physics 127 (2024103) (2007) 1–10. doi:10.1063/1.2747249.  
URL <http://aip.scitation.org/doi/10.1063/1.2747249>
- [6] E. Longo, E. Orhan, F. M. Pontes, C. D. Pinheiro, E. R. Leite, J. A. Varela, P. S. Pizani, T. M. Boschi, F. Lanziotti, A. Beltrá, J. André, Density functional theory calculation of the electronic structure of Ba<sub>0.5</sub>Sr<sub>0.5</sub>TiO<sub>3</sub>: Photoluminescent properties and structural disorder, Physical Review B 69 (125115) (2004) 1–7. doi:10.1103/PhysRevB.69.125115.  
URL <https://journals.aps.org/prb/pdf/10.1103/PhysRevB.69.125115>
- [7] D. Hohl, R. O. Jones, First-principles molecular-dynamics simulation of liquid and amorphous selenium, Physical Review B 43 (5) (1991) 3856–3870. doi:<https://doi.org/10.1103/PhysRevB.43.3856>.  
URL <https://journals.aps.org/prb/abstract/10.1103/PhysRevB.43.3856>
- [8] Y.-J. Zhang, J.-H. Lan, C.-Z. Wang, Q.-Y. Wu, T. Bo, Z.-F. Chai, W.-Q. Shi, Theoretical Investigation on Incorporation and Diffusion Properties of Xe in Uranium Mononitride, The Journal of Physical Chemistry C 119 (11) (2015) 5783–5789. doi:10.1021/jp510219a.  
URL <http://pubs.acs.org/doi/10.1021/jp510219a>
- [9] B. Dorado, M. Freyss, B. Amadon, M. Bertolus, G. Jomard, P. Garcia, Advances in first-principles modelling of point defects in UO<sub>2</sub>: f electron correlations and the issue of local energy minima This, Journal of Physics: Condensed Matter 25 (333201) (2013) 1–13.

- [10] J. Y. Raty, W. Zhang, J. Luckas, C. Chen, R. Mazzarello, C. Bichara, M. Wuttig, Aging mechanisms in amorphous phase-change materials, *Nature Communications* 6 (7467) (2015) 1–8. doi:10.1038/ncomms8467.  
URL <http://dx.doi.org/10.1038/ncomms8467>